16.2 Surface Treatments to Gain Desired Properties: Coating, Polishing, Patterning

There are various ways to improve the stent design in order to make it more effective. One way is coating the surface with organic and inorganic materials. This is not trivial with the complex geometry of the stainless steel mesh. Nevertheless this route is extensively studied given its benefit of incorporating drugs into the polymer-based surface coating which can be eluted over time into the surrounding vessel material. However, there are several reasons, including concerns about increased risks of late stent thrombosis when using drug-eluting stents [8, 9], why the development focus is likely to return to bare metal or polymer-free stent technologies [3].

While from the invention of stents it was aimed for a surface as smooth and polished as possible in order to minimise abrasion and inflammation of the body tubes, it becomes ever more apparent that a somewhat roughened/textured surface might be a better fit for the task.

16.3 Biomaterial–Cell Interaction: Advantages of Rough/Patterned Surfaces

The influence of textured material surfaces on the behaviour of cells has been studied for many years by now [10–16]. On one hand, theoretical studies show that cells prefer to grow on rough surfaces in general as it imitates best naturally occurring surfaces [17]. On the other hand, in order to have a better control over and to minimise the complexity of the experimental conditions, the natural urge to study regular patterns led scientists from rough to micro- to nano-patterned surfaces. Especially in tissue engineering where the tissues involved require certain mechanical and structural properties for proper functioning, the trend from micro- to nano-structured surfaces serving as artificially created support systems has become evident within the last decade [18–24]. Also for drug delivery the control over biointerfacial interactions is often the key to biomedical applications [14].

In particular endothelial, smooth muscle and fibroblast cells play an important role in the healing process and maintenance of cardiovascular systems and thus are likely to be in contact with biomedical implants such as stents and grafts. During a surgical procedure involving the introduction of a stent, vascular tissues in the arteries may be damaged. Healing of vascular tissues is promoted by the formation of an endothelial cells lining on the stent substrate [25], while the presence of smooth muscle cells and fibroblasts may cause re-stenosis. Micro- and nano-textures on substrates may provide control of cell functions. Such structures could promote better vascular cell adhesion, decrease the need for systemic administration of drugs and reduce the requirement for secondary surgery after stent implantation.

16.4 Patterning: Lithography, Electrodeposition, Dip Pen, Pulsed Laser, FIB

Recent advances in micro- and nanotechnology have allowed the patterning of surfaces with the desired textures for cell scaffolding [26–29]. Nano-texturing involves the creation of patterns or features with nanometre precision. The choice of the texturing method depends largely on the nature of the substrate that needs to be modified and on the dimensions of the features expected. Indeed, photolithography was particularly successful for the patterning of features of microscopic dimensions on elastomers such as polydimethylsiloxane (PDMS) [30–33] and on polymers such as polystyrene (PS) [34–37]. E-beam lithography was used for the patterning of submicron features on silicon substrates [38, 39] and on poly(methyl methacrylate) (PMMA) [40]. Features of 350 nm were patterned on PDMS and PMMA substrates by nanoimprint lithography [41]. Metal substrates such as Ti were also textured using micro-machining for feature dimensions in the microscopic range [10, 42]. Cell adhesion, migration, elongation, proliferation and gene expression on textured substrate can be greatly altered depending on the shape and the dimension of the features [40].

The different techniques are compared in Table 16.1. In indirect photolithography methods, patterns are formed over a large area using a mask [43]. Such lithography processes are time consuming with many steps and inherently inappropriate for prototype designs and processes. Electrodeposition is a simple, fast and cost-effective method of reproducing nano-structures on many materials using templates made of polymers and metals. However, this method is applicable only for electrically conductive substrates. Imprint lithography is a high-resolution direct technique for nano-patterning of large surfaces, but it requires moulds and is restricted to polymeric materials [44], but this could then be used as etch masks or filled with metal electrodeposition. E-beam lithography and lithography based on scanning tunnel microscopy (STM), atomic force microscopy (AFM) or dip pen are high-resolution mask-less procedures, but with a very low throughput and unsuitable for wide surface nano-patterning [45]. Interference lithography can be utilised to create or transfer array patterns on various metallic and polymeric surfaces, but only patterned features can be reproduced. Microtexturing of surfaces has also been reported by pulsed laser patterning [46, 47]. The feature sizes are however limited to the micron range.

Patterning by FIB milling is direct and offers several advantages for flexible prototyping: (1) practically any substrate material that is able to withstand high vacuum conditions of the microscope chamber can be used, (2) there is high flexibility in the obtainable shapes and geometries by modulating the ion beam current and the patterning conditions, (3) reduced complexity of the patterning process, e.g. it is a single-step process with a possibility of real-time monitoring of the milling progression. Thus for any particulate type of substrate, various depths as well as lateral dimensions including the optimal feature size can be obtained at minimum number of processing steps.

t1.1 **Table 16.1** Advantages and disadvantages of indirect and direct nano-structuring techniques

t1.2 t1.3 t1.4 Mask/ moulds required	Nano-fabrication techniques	Advantages	Drawbacks
t1.5 Yes	Photolithography	Well-controlled features	Requires photoresist, spin coaters and organic solvents Low aspect ratio
t1.6 t1.7		High throughput	Limited to set of materials
t1.8 t1.9	Electrodeposition	Precise geometries and patterns	Require templates for creating of nano-structures
t1.10 t1.11		Large surface area	Limited to electrically conducting substrates
t1.12	Imprint lithography	High resolution	Requires moulds
t1.13 t1.14		High aspect ratio Large surface	Applied to polymers only
t1.15 No	E-beam	High resolution	No direct writing on substrate
t1.16		Precise geometry and patterns	Multistep process
t1.17			Low throughput
t1.18			Requires vacuum
t1.19			Time consuming
t1.20			Small surface coverage
t1.21			Expensive
t1.22	Interference lithography	No complex optical systems	Limited to patterned array features only
t1.23			Multistep process
t1.24	STM/AFM/ dip pen	Very high resolution	Low aspect ratio
t1.25			Very low throughput
t1.26			Very small surface area
t1.27	Nanoindentation	High aspect ratio	Wide and shallow features
t1.28		Control over features depth	Slow process
t1.29 t1.30		Less expensive than FIB or e-beam writer	
t1.31	Laser patterning	Any material	Wide and shallow features
t1.32 t1.33		High throughput with high power laser	Micron resolution
t1.34	FIB milling	High resolution	Time consuming
t1.35		High aspect ratio	Process requires vacuum
t1.36		High etch rate	Very expensive
t1.37		Any material	Low throughput

16.5 FIB Advantages: Fast for Prototyping 126

Except FIB, none of the texturing techniques mentioned above were suitable to 127
achieve features in the nanoscopic range on a hard substrate as 316L stainless steel. 128
Nanoimprint lithography (NIL) and e-beam lithography (EBL) are able to pattern 129
submicron features, which with NIL were achieved on soft substrates such as poly- 130
mers and elastomers only and with EBL is a very time-consuming and expensive 131
multistep process. In this research work, FIB milling was used to create 132

nano-structures onto stainless steel because it is a direct writing process with simple steps, high resolution and aspect ratios. Nano-structured features such as pits were created on 316L steel surfaces. The optimal FIB patterning conditions for achieving reasonably high throughput (patterned rate of about 0.03 mm^2/h) and nano-size accuracy in dimensions and shapes of the features are discussed. Additionally, a characterisation protocol for analysis of such structures by combination of electron backscattering diffraction (EBSD), FIB, scanning electron microscopy (SEM), atomic force microscopy (AFM) and serial FIB–SEM sectioning is detailed. Furthermore, this chapter reports the comparison of in vitro EC adhesion and growth on FIB nano-structured, unpolished and electropolished 316L steel surfaces.

16.6 FIB Overview: Ga^+ Beam, Maskless, Pattern Design

FIB systems usually employ a finely focused beam of gallium ions (Ga^+) that can be operated at high beam currents for milling or low beam currents for imaging. It can be utilised to remove material locally in a highly controlled manner to the nanometre scale. When the high-energy Ga ions impinge the sample, atoms from the sample surface are sputtered. In addition, Ga atoms from the ion beam are also implanted into the top few nanometres of the surface, and the surface is made amorphous. As can be seen in Fig. 16.2, the Ga^+ primary ion beam hits the sample surface and sputters a small amount of material. The primary beam also generates secondary electrons. When the primary beam strikes the sample surface, the signal from secondary electrons or sputtered ions is collected to form an image of the surface [48].

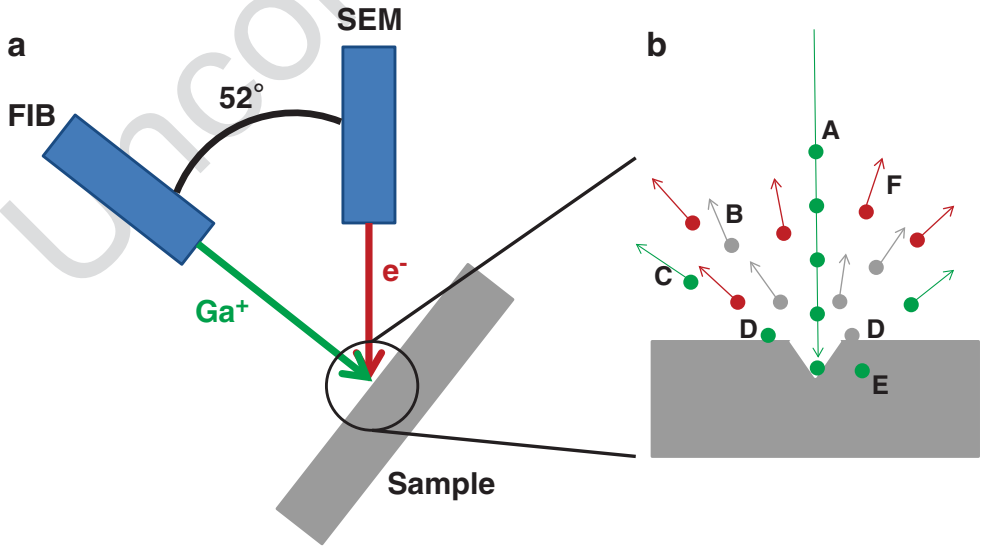

Fig. 16.2 (**a**) Dual-beam FIB schematics. (**b**) Beam sample interactions: *A*—incident Ga^+ ions, *B*—sputtered substrate atoms, *C*—scattered Ga^+ ions, *D*—re-deposited Ga^+ ions and substrate atoms, *E*—in substrate trapped Ga^+ ions and *F*—secondary electrons

At a low primary ion beam current, a minuscule amount of material is sputtered, and with existing FIB methods, 5 nm resolution can be attained using Ga ions. However, at higher primary ion beam current, a considerable quantity of material can be taken out, which allows sub-micrometre- to nanometre-scale precision milling of sample surface.

FIB originated in the semiconductor industry and has become an important tool for a wide array of applications, ranging from circuit editing, reverse engineering, sample preparation for transmission electron microscopy (TEM), microstructural analysis and prototype nanomachining to name just a few [49]. Many modern FIB instruments supplement the FIB column with an additional SEM column so that it becomes a versatile dual-beam platform as depicted in Fig. 16.2. In nano-patterning, FIB has been used to create nano-structures on Si [50], silicon nitride [48, 51] and glass substrates [52] and to fabricate platinum nano-structures on peptide-based soft surfaces [53]. Only one study reported the protein adsorption on FIB patterned glass surfaces [52]. To date, no cellular studies have been reported on FIB-structured surfaces. Moreover, this and other aforementioned techniques have not been employed for patterning the key vascular stent material 316L stainless steel for vascular cell functions. Studies do not exist that determine the EC response on 316L steel with nano-pit features. Endothelial cell studies on unpatterned 316L stainless steel substrates have shown that the grain size and grain boundaries have an impact on their adhesion and morphology [54]. Chemically etched substrates with 16 μm grain size etched have demonstrated cell densities significantly higher than with grain sizes of 31, 47 and 66 μm. The authors attribute this increased cell density to greater boundary area and associated higher surface free energy [54]. Cell proliferation was also subject to another study discussing different materials. There the grain sizes varied from 320 nm to 22 μm. Again cell proliferation was reciprocal dependent on the grain size [55].

16.7 Crystal Structure of Stainless Steel 316L

Austenitic type 316L stainless steel is commonly used for manufacturing medical implants [56] and was hence selected as the substrate of choice for this study. Austenitic stainless steels have face-centred cubic (fcc) crystal structure, in which the unit cell is a cube with atoms located at the corners and middle of each side (Fig. 16.3a). The presence of higher concentration of Ni in austenitic stainless steels stabilises the fcc crystal structure, because Ni is a fcc crystal itself. This enhances the ductility, i.e. it can sustain large plastic deformation without fracture compared to other stainless steels (maternistic and ferritic phases). [AU2]

Most metallic materials are composed of many small single-crystalline planes called grains. These materials are referred to as polycrystalline materials (e.g. steel), in which individual grains have identical arrangement of atoms but the orientation of the atom arrangement or crystal structure is different from each adjoining grain (see Fig. 16.3b for visualisation). The interfaces between these grains are grain boundaries, the surface that separates the individual grains [57].

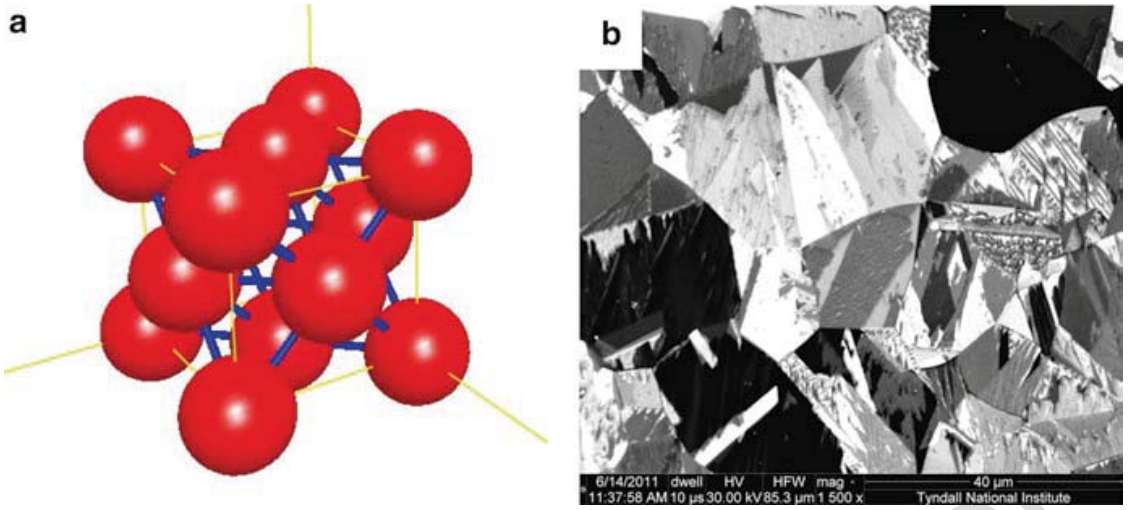

Fig. 16.3 (**a**) Schematic face-centred cubic crystal structure and (**b**) FIB image of polycrystalline 316L used in this study

The austenitic stainless steel function can be affected by two microstructure features: grain (or crystal) size and shape. The general grain size suggested for 316L is 100 µm or less [56]. This is because smaller grains have more grain boundaries, which provide resistance to plastic deformation as they are responsible for slip deformation by dislocations.

Depending on the process conditions such as annealing and cold-working, the shape of austenitic stainless steel grains varies. Annealing is a heat treatment process where a material is modified, resulting in changes in its properties, for example, strength and hardness. It is a method that generates conditions via heating to above the recrystallisation temperature, maintaining an appropriate temperature, and subsequently cooling. This method is applied to reduce internal tensions, soften material, [AU3] enhance ductility, improve the structure by creating it uniform and enrich cold-working properties. Austenite grains of the stainless steels under an annealed condition exhibit an equiaxial granular shape (i.e. the grains having axes of equal length).

Cold-working produces plastic deformation in the steels and generates a strain hardening effect, which improves both yield strength and tensile strength of steel considerably. However, in cold-worked steel, depending on the amount of cold work, the grains are elongated (i.e. longer in the rolling direction). During large plastic deformation, textured grain structures are produced and preferentially align the grains in specific crystallographic orientations. Hence, cold-worked steel with textured structures demonstrates anisotropic mechanical properties. When employing a cold-worked steel for implant fabrication, microstructure analysis is suggested as implants can be better prepared if the loading direction is concurrent to the high strength direction in the steel [56]. Hence, it is clear that the microscopic and crystalline structure can play a strong role on the nano-structuring of the stainless steel surface.

16.8 Substrate Preparation: Electropolishing, Cleaning

Electropolished 316L steel substrates were used for this study. Figure 16.4 illustrates the steps involved in the whole sample process flow. Electropolishing of steel was performed with a view to the preparation of these surfaces for nano-texturing. For such applications, a smooth surface is crucial. The composition of this electrolyte solution was 11 M H_3PO_4 + 4.5 M H_2SO_4 in water. The electropolishing procedure was conducted in two steps at 80 °C and 5 mV s^{-1} [58]. The first step involved scanning of the potential from the open-circuit potential up to the point where the diffusion-limited current region was reached. The linear sweep voltammetry was then stopped, and the selected potential was maintained 10 min using chronoamperometry. This resulted in a smooth and relatively defect-free surface. XPS analysis of the electropolished surface has shown that the stainless steel was enriched with Cr, P, S, O, Mo and Ni elements. Prior to nano-structuring, the polished specimens were cleaned in acetone, in ethanol and finally in ultrapure water via an ultrasonic treatment for 10 min.

16.9 FIB Tests: Challenges with Anisotropic Milling

The FIB system used in the current study is the FEI Helios NanoLab 600i, which is a dual-beam FIB for localised milling and deposition, transmitting a 30 keV beam of Ga^+ ions combined with a high-resolution SEM. In this work, the working current was tuned between 0.28 nA (for 120 nm pits) and 0.92 nA (180 nm) depending on size of the nano-texture. The available pit sizes and the large range of obtainable working currents could make the FIB technique an ideal device for nanomachining in the range from 10 nm to a few micrometres. Nano-structured features (pits/holes) ordered in rectangular arrays were patterned on 316L steel surfaces using FEI Helios NanoLab 600i FIB system. This system was used because of high beam quality and stage stability.

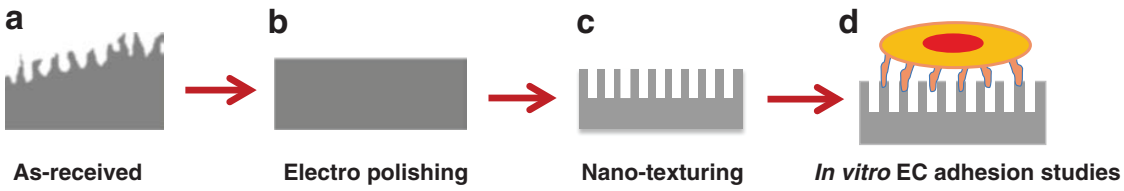

Fig. 16.4 Sample process flow in total. (**a**) Samples as received with rough surface. (**b**) Electropolishing to obtain a smooth surface suitable for nano-structuring. (**c**) Nano-texturing of 316L stainless steel via a focussed ion beam (FIB) milling. (**d**) In vitro endothelial cell adhesion studies

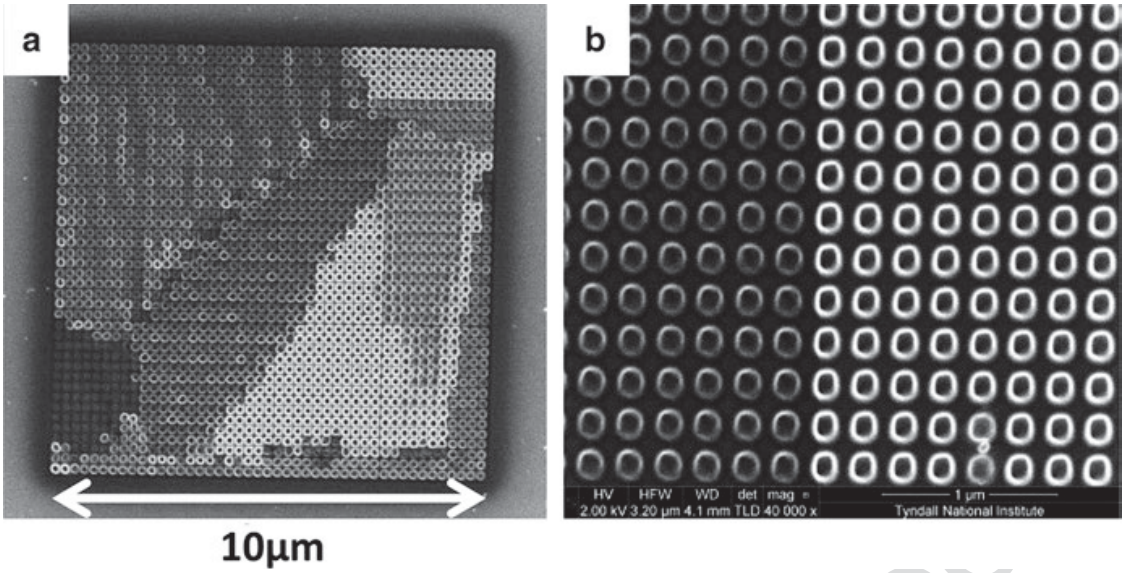

Fig. 16.5 SEM images of preliminary FIB tests to determine the feasibility of the prototyping approach. (**a**) 10×10 **µ**m area pattern by FIB in preliminary tests with nominal 120 nm wide pits at 240 nm pitch. (**b**) Detail of another area exhibiting the same pattern. Clearly visible are the differences in appearance of the patterned surface depending on the polycrystallinity of stainless steel

From the literature survey, promising cell responses to nano-structured features were identified including nano-pit features [40, 59]. However, to date no EC studies have been reported on nano-pit structures. Based on this, two pit designs were patterned on three electropolished 316L stainless steel samples on areas of 400 µm×400 µm using FIB: design A, pits of 120 nm diameter with a pitch of 240 nm and intended depth of 50–100 nm, and design B, pits of 180 nm diameters with pitch of 360 nm and intended depths of 50–100 nm [60, 61].

Before attempting prototyping on large 400×400 µm areas used for the biological tests, we have performed optimisation tests on relatively small test patterns; one such area is shown in Fig. 16.5a. From the known polycrystalline nature of the 316L stent material, one can assume that when subjected to ion milling or imaging, it will show pronounced channelling contrast. It is well known for about a century for W, Ag or Cu which are all fcc metals that they etch and sputter faster in preferred directions [62–65], as well as Si [66, 67]. Similarly polycrystalline fcc austenitic stainless steel will show milling rates that are varying by the different orientation of grains towards the incoming beam.

Figure 16.5 illustrates how much this anisotropic milling affects the desired outcome of uniform concaves. Shown in Fig. 16.5 are examples from the pretests on 10 µm×10 µm areas with 120 nm diameter holes at 240 nm pitch. The structures that appear with the brightest contrast showed deeper and sharper edges than the structures that appear darker in contrast. This will be discussed in more detail in the following section describing the correlative microscopy approach. A later section will focus on the study on the patterned substrates used for actual cell adhesion tests and the preliminary FIB tests.

16.10 Correlative Microscopy: EBSD, FIB, SEM, AFM, and Serial Sectioning FIB–SEM Towards Better Understanding of Beam–Substrate Interaction

In order to gain a better understanding of the beam–substrate interaction during patterning, a correlative microscopy approach was used to illuminate the patterning process from many possible angles [68, 69]. This was also done on a batch of samples that could not be used for the cell adhesion studies basically because of the destructive nature of the last step, the serial FIB–SEM sectioning.

The different techniques used for the characterisation of nano-textured, unpolished and electropolished stainless steel surfaces were electron backscattering diffraction (EBSD), FIB, SEM, atomic force microscopy (AFM) and serial FIB–SEM sectioning. Figure 16.6 shows the detailed process flow of the correlative approach.

EBSD technique was used to analyse the crystallographic structured surfaces of the polished stainless steel. EBSD imaging was performed in a Hitachi SEM SU-70 equipped with an Oxford Instruments EBSD attachment AztecHKL at 10 kV under 70° tilt angle and step size 2 μm.

FIB technique was also used to visualise the crystallographic structured surfaces of the polished stainless steel. FIB imaging was performed as a part of monitoring of the milling at 30 kV accelerating voltage.

SEM was used to analyse the topography of nano-textured surfaces of the polished stainless steel. The SEM images presented were obtained using a SEM at the FEI Helios NanoLab 600i at an electron beam current of 5 kV and 86 pA beam current.

A commercial atomic force microscope (MFP 3DTM, Asylum Research) in AC mode was used for topography mapping of the films. Olympus AC160TS silicon cantilevers (Al reflex coated, ~300 kHz resonant frequency) were used for imaging. Optimal results were achieved with a medium scan rate of 1 Hz and 256×256 pixels image resolution.

Samples for serial sectioning were prepared using protective carbon and Pt layers [70]. The electron beam-induced (EBID) carbon deposition supplied necessary contrast difference between the protective Pt and the stainless steel surface, hence enabling accurate determination of the concave's shape and depth.

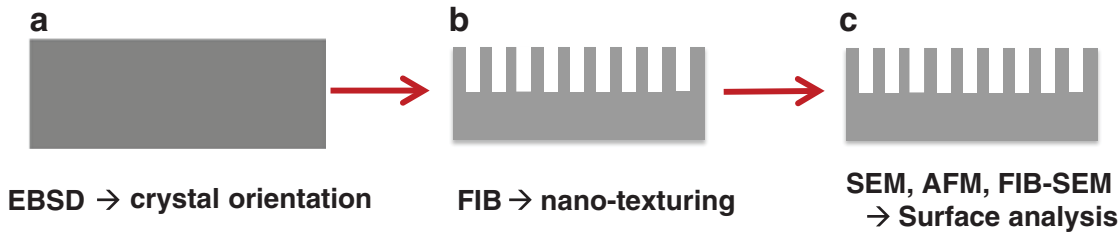

Fig. 16.6 Process flow in the correlative microscopy approach. (**a**) The crystallographic grain orientations are measured by EBSD before patterning. (**b**) Surface patterning using FIB, also gaining FIB SE images as part of the monitoring process. (**c**) Extensive analysis of the textured steel surface with SEM, AFM and finally destructive serial FIB–SEM sectioning

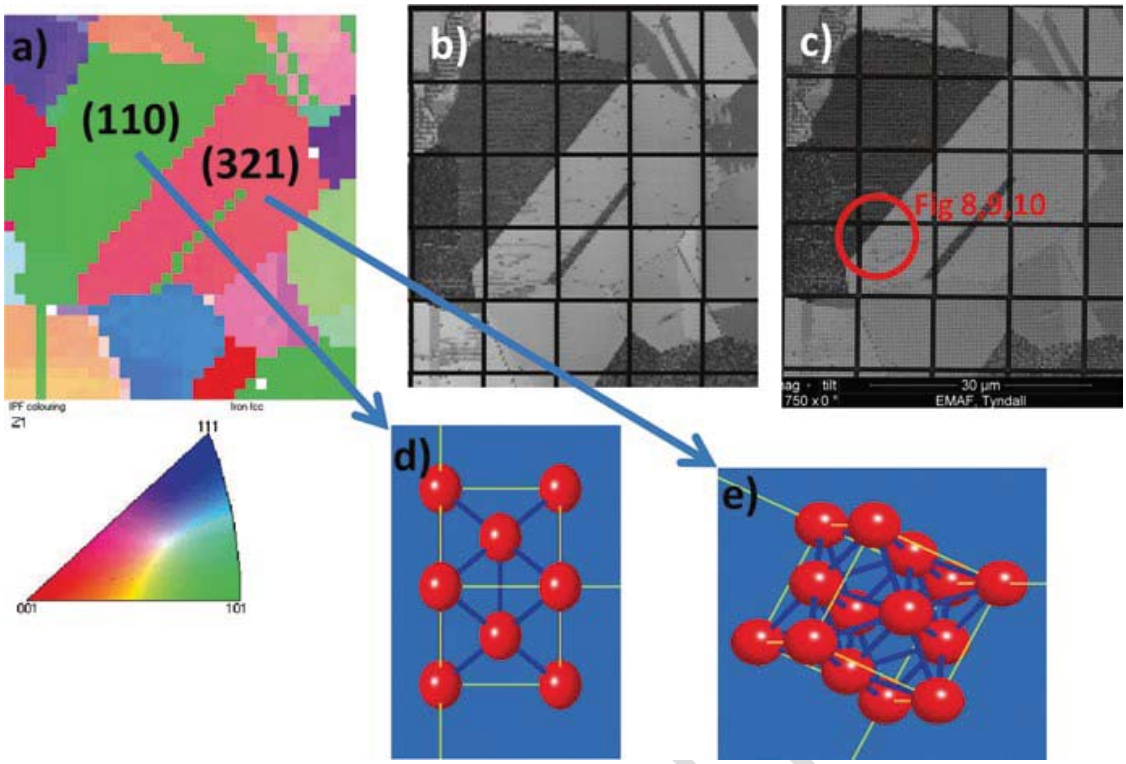

Fig. 16.7 Correlative microscopy on the exact same sample location. (**a**) Inverse pole figure (IPF) as measured by EBSD before surface texturing with (110) and (321) crystal orientation labelled and legend underneath. (**b**) FIB SE image obtained during patterning as part of monitoring. (**c**) SE image taken after the patterning—the *red circle* indicates the region used for AFM and serial sectioning (see Figs. 16.8, 16.9 and 16.10 for details). (**d**) Graphical visualisation of (110) orientation. (**e**) Graphical visualisation of (321) orientation

EBSD is an SEM-based microstructural–crystallographic technique to measure individual grain orientations, local texture, point-to-point orientation correlations and phase identification and distributions on the surfaces of bulk polycrystals. It is also known as backscatter Kikuchi diffraction (BKD), and both acronyms are being used interchangeably in the literature. EBSD patterns are generated on a phosphor screen by backscatter diffraction of a stationary beam of high-energy electrons from the typically 70° tilted sample surface. Because of the high tilt angle—or the shallow 20° angle of the incident beam towards the surface—this technique is very surface sensitive and gives information of the top 20 nm down into the substrate [71].

EBSD mapping was accomplished before the area was patterned in order to determine a correlation between crystal grain orientation on one hand and shape, size and depth of the FIB-milled concaves on the other hand. Figure 16.7 shows the random size and orientation of the crystal grains and illustrates the correlative microscopy approach of three techniques combined in the exact same sample location, EBSD, FIB and SEM. In general the intensity of the emitted SE depends on the different inclination of the sample surface towards the incoming beam and crystal orientation [72]. Thus, the grey levels in the SEM image are directly linked to the

surface topography, e.g. the shape of the pits and sidewall profile and the crystal orientation of the surface material. In this way we can correlate the EBSD data to the grey levels in the SEM images. The FIB reveals not surprisingly the same contrast in the SE image as the one taken afterwards in the SEM. The SE yield is independent of the type of the beam; hence the same contrast is achieved. The additional information of the SEM SE image lies in the much higher resolution. The FIB which was run as a monitoring tool only during the patterning process produced one pixel every 360 nm in *X* and *Y* direction. The SEM on the other hand was used afterwards as an analysis tool with an image resolution of 4,096×3,775 pixels which calculates at roughly 3 nm image resolution. Using a low current of 86 pA ensured that the real resolution is not far from this theoretical limit.

Two different grains were chosen for additional correlation with AFM and the serial FIB–SEM sectioning based on the crystallographic orientation, a low index grain with (110) orientation and a high index grain with (321) orientation. From as early as the 1920s, it is known that the sputter yield is dependent on the crystal orientation [62]. It is also known that the SE yield is dependent on the crystal orientation [72]. Based on this fact the chosen grains should display a very different behaviour when exposed to the ion beam during sputtering and also to the electron beam in the SEM study.

Studying the marked region from Fig. 16.7 across the grain boundary using the AFM (see Fig. 16.8), it appears that there is a difference in hole depth and diameter depending on crystallographic orientation of the patterned surface. Even the shape of the rim is evidently not circular but rather rhombohedral. Because of the high aspect ratio of the pits, the tip could not reach down and probe the full depth of the pits; therefore, the pit depth must be confirmed by the serial sectioning.

The first that comes to mind when seeing the rhombohedral shape of the pits is the directional dependence in which atoms are ejected when sputtering at threshold energy [63]. In our study however the energy used to create the patterned surfaces in the FIB was way beyond the threshold energy, which for Cr, Ni and Fe as main elements in 316L lie in the range of 60–90 eV. The directional dependence decreases with higher sputter energies and has no influence on the direction of the sputtered atoms at the 30 keV used here. It is also obvious when looking in detail at the (111) oriented grain at the bottom of the AFM overview scan that shows the same rhombohedral-shaped pits as the whole area around this region instead of the expected triangular shape. As can be seen below in the detailed AFM and SEM studies on the 400 µm×400 µm patterns used for the cell adhesion studies, the shape of the holes is solely determined by the ion beam quality (focus, stigmation) at the place of impact on the sample surface.

In the SEM surface study as depicted in Fig. 16.9a, it appears as if the holes in both grains seem equal in diameter with only the higher SE yield obvious for the higher index grain. In order to clarify this impression, the region was imaged again after depositing a carbon layer as shown in Fig. 16.9b. Because secondary electrons are emitted from an area very close to the surface of the sample, this amorphous carbon layer masks the crystal orientation of the sample surface, and the image is

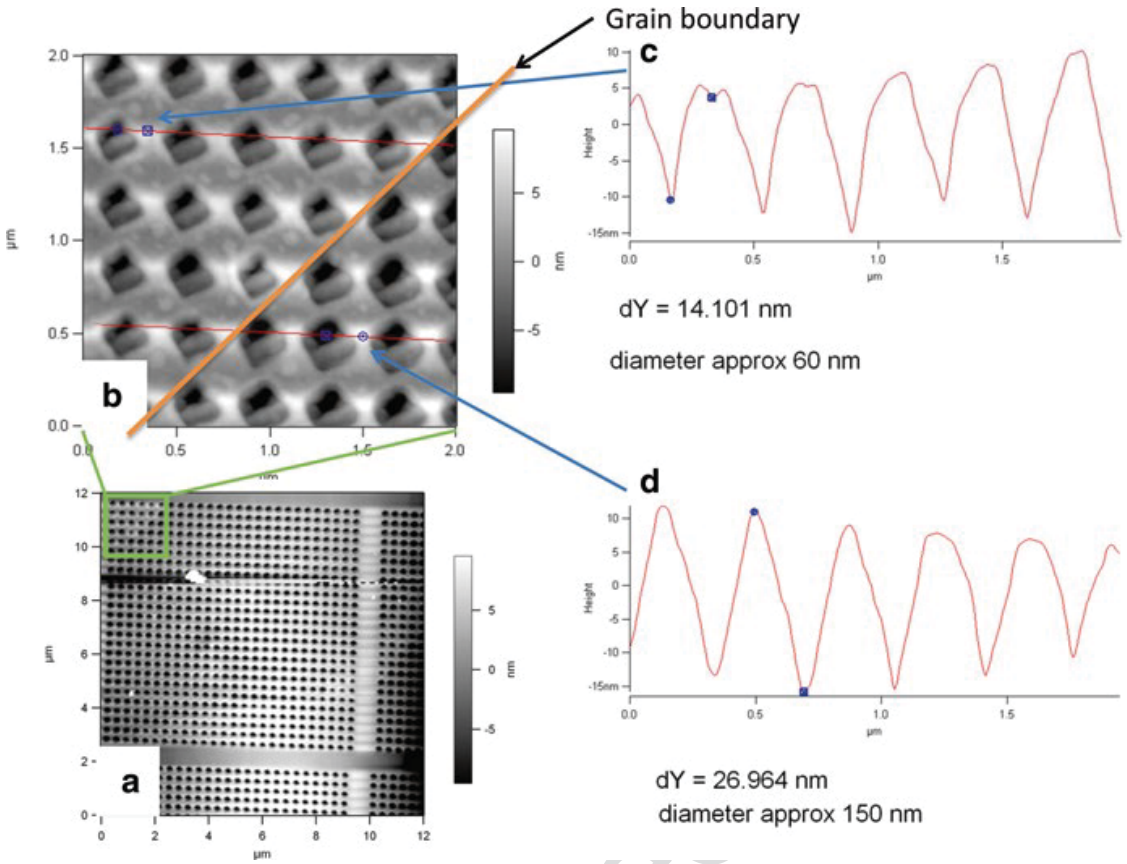

Fig. 16.8 Representative AFM scans of the marked region from Fig. 16.7. (**a**) Overview scan over the whole 12 µm × 12 µm region. (**b**) Detailed 2 µm × 2 µm scan of the area around the crystal grain boundary. (**c**) Line profile along one row of five holes determining depth and diameter of the holes in the (110) oriented grain. (**d**) Same line profile determining the depth and diameter of the holes in the (321) oriented grain

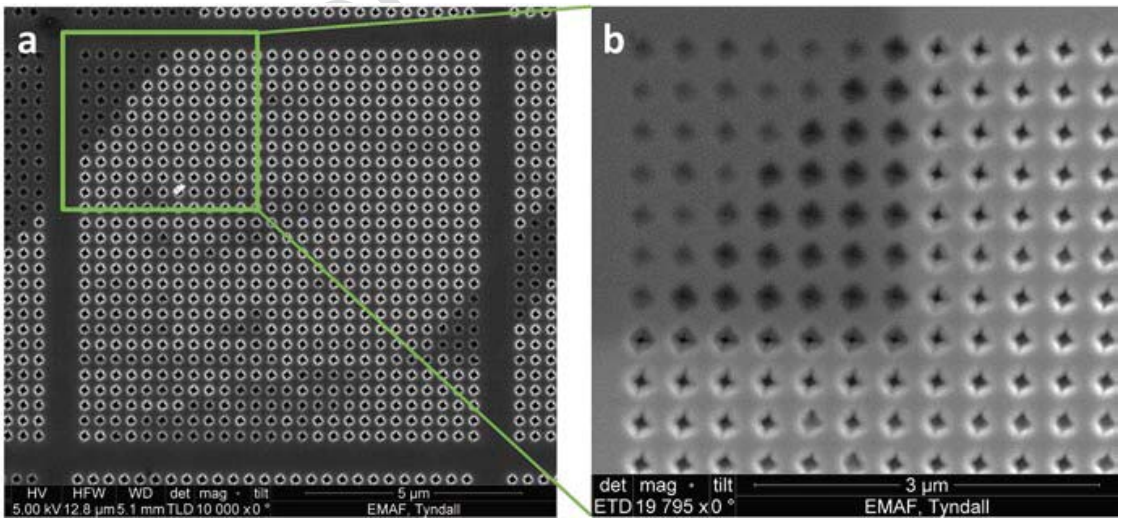

Fig. 16.9 Detailed SEM images of patterned area marked by the *red circle* in previous picture. (**a**) Freshly patterned surface displays high SE yield for the high index grain and low yield for the low index grain, though the holes seem equal in diameter. (**b**) Detail of (**a**) after carbon deposition, the "true" diameter shines through as crystal orientations are hidden behind the amorphous carbon layer

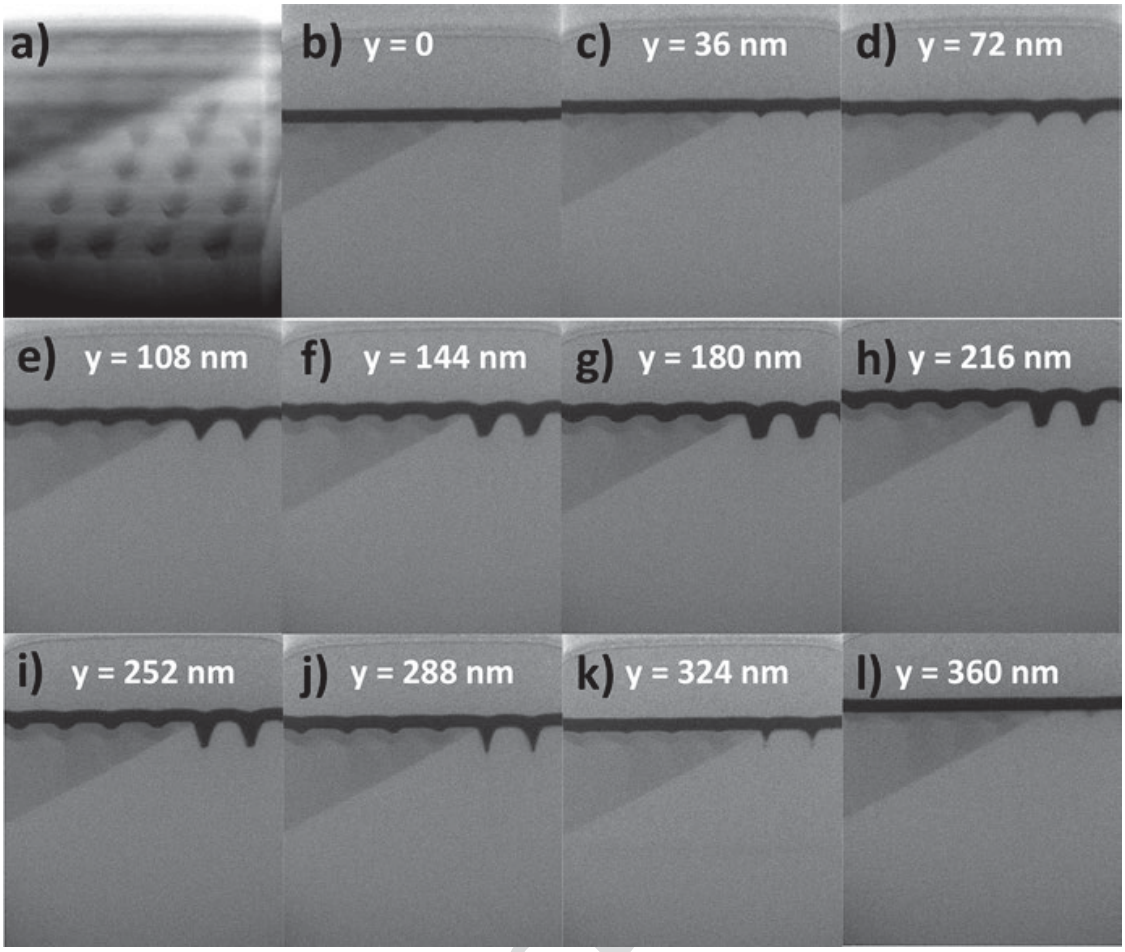

Fig. 16.10 Serial sectioning as final destructive step of the correlative microscopy. (**a**) 3D reconstruction of all the 250 slices. (**b–l**) Image series illustrating one row of six holes taken every 36 nm (every third image). The *darker left* region is the low index grain (110) oriented, the *brighter right hand side* is the higher index (321) oriented grain. Obvious is the difference in depth by more than a factor of 3 between the two patterned grains

more related to topographical features. Indeed, the difference in diameter of the holes becomes pronounced, and it is visible that the higher index grain has apparently much larger holes than the lower index grain.

Serial sectioning of again the same region was performed composing 250 images of 8 rows by 5 holes, with one image taken every 12 nm. This detailed analysis verifies the difference not only in the diameter but even more pronounced in the depth. Though Fig. 16.10a presents a 3D reconstruction of all the 250 slices, more details can be observed when looking at the individual slices of Fig. 16.10b–l. The diameter of the pits in the low index (110) oriented grain are 150 ± 10 nm, while the diameter in the (321) oriented grains is only slightly bigger with 170 ± 10 nm. The depth however is much more influenced by the differences of sputter yield depending on the crystal orientation, and hence the (110) grain shows only 55 ± 5 nm depth in contrast to the 200 ± 20 nm depth of the (321) grain, nearly a factor of 4 between them.

16.11 Prototyping: Samples Prepared for Cell Adhesion Tests and Statistical Pattern Analysis

After the initial tests for the feasibility of the patterning was finished successfully on the batch of samples with small-scale pattern, the "real" prototyping on the 400×400 µm patterned areas had been started. As consensus between statistical needs for ideally a high number of samples on one hand and the slow process of patterning with the FIB on the other hand, five samples with each one area of 120 nm pits/240 nm pitch and one area of 180 nm pits/360 nm pitch were manufactured.

The two pit designs, A and B, were created on electropolished stainless steel samples by FIB and are presented in Fig. 16.11. Three things can be observed. First, the square areas that have been milled by the FIB are very different from the electropolished areas. Second, the triangular areas in the centre are much better defined than the areas at the edges. Finally, within and outside these triangular areas, the different colour tones observed are due to the polycrystallinity of the stainless steel as described in detail in the previous section.

Alternatively, AFM was used to evaluate statistically in more depth the information on topography, pit feature dimensions and as a comparison of the results obtained via serial FIB–SEM sectioning. AFM examinations for this analysis were performed in tapping mode using a Dimension 3100 with a Nanoscope IIIa controller equipped with a phase imaging extender (Digital Instruments, Santa-Barbara, CA, USA). The silicon cantilevers (purchased from Windsor Scientific, UK) have a tip radius of less than 10 nm and a 40 N m^{-1} spring constant. AFM images were

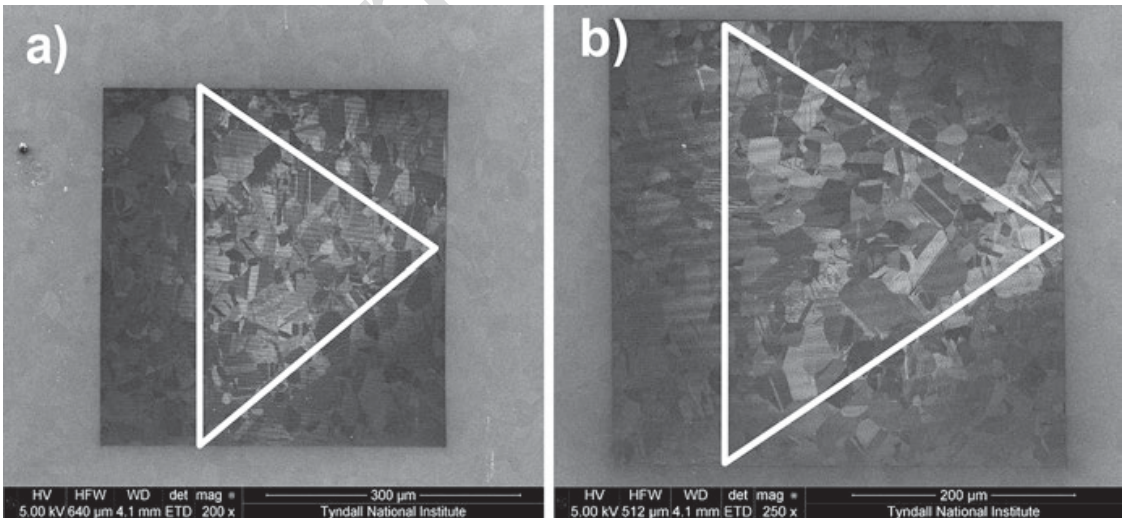

Fig. 16.11 Overview of SEM images of (**a**) design A and (**b**) design B showing (1) differences in milled (*inside* the *square* area) and electropolished surfaces (*outside* the *square* area), (2) *triangular* areas covering more than half of the 400 µm×400 µm *square* are much better defined than the areas at the corners in the *squares* and (3) different colour tones illustrate the polycrystallinity of the stainless steel

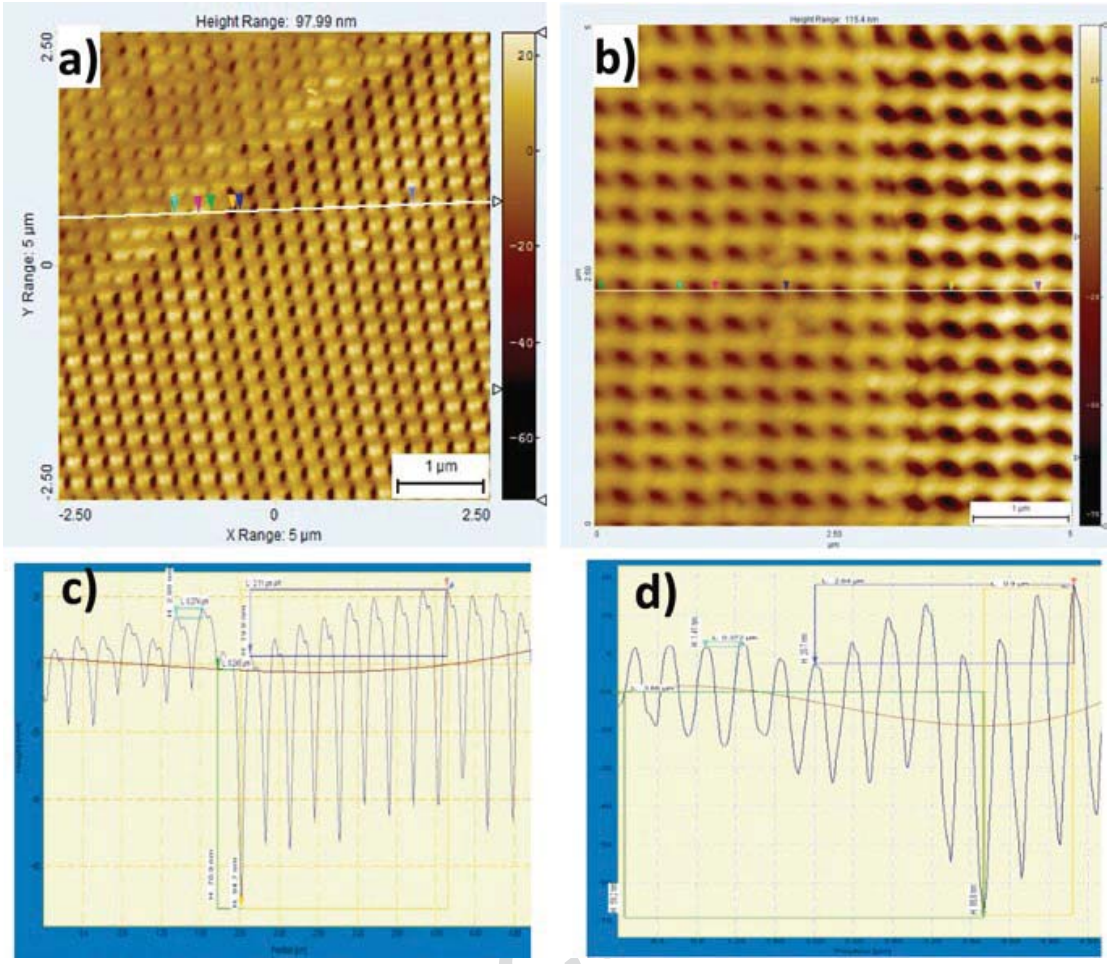

Fig. 16.12 AFM top view and cross-sectional images of pits (**a**, **c**) design A and (**b**, **d**) design B. Variation in depth dimensions from AFM profiles in region I and II is clearly noticed

recorded at a scan rate of 0.5 Hz and a resonance frequency of 300 kHz. Each sample was evaluated over scan fields of 5×5 µm², 1×1 µm² and 500×500 nm². The pit dimensions of the resulting images were evaluated using scanning probe imaging processor software (version 5.1.5).

Four nano-structured samples were used for the measurements. Four topographic measurements were performed in different random fields per substrate. Figure 16.12 shows the 2D AFM images and profiles of designs A and B on 5×5 µm² areas. A similar trend was noticed with AFM data. Region I showed shallower structures than region II, Fig. 16.12a, b. From the AFM profiles across a 5 µm width as depicted in Fig. 16.12c, d, the average depth recorded in region I for design A and design B was 24±18 nm and 26±20 nm (N=115), whereas in region II the average depth was 68±48 nm and 64±8.5 nm (N=115). This variation of more than four times indicates that an exact match of the desired depth of 50–100 nm can only be approximated.

The images presented in Fig. 16.13a, b are of a closer SEM inspection of designs A and B on triangular areas of 5×5 µm². The pit structures within the triangular zones are circular as wanted for pit designs A and B (Fig. 16.13a, b).

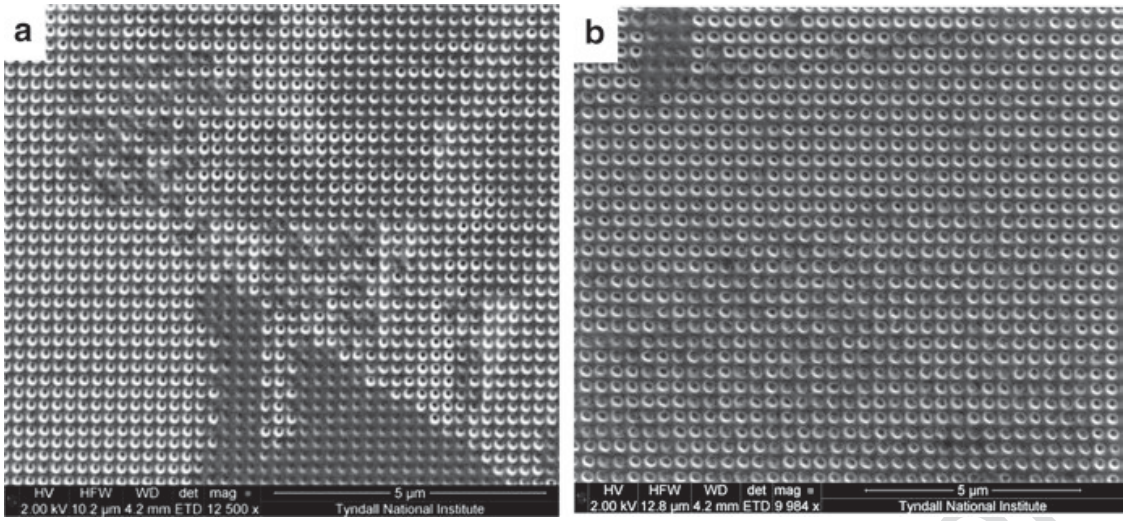

Fig. 16.13 SEM images of circular pits of (**a** and **b**) design A and B reproduced within the triangular areas

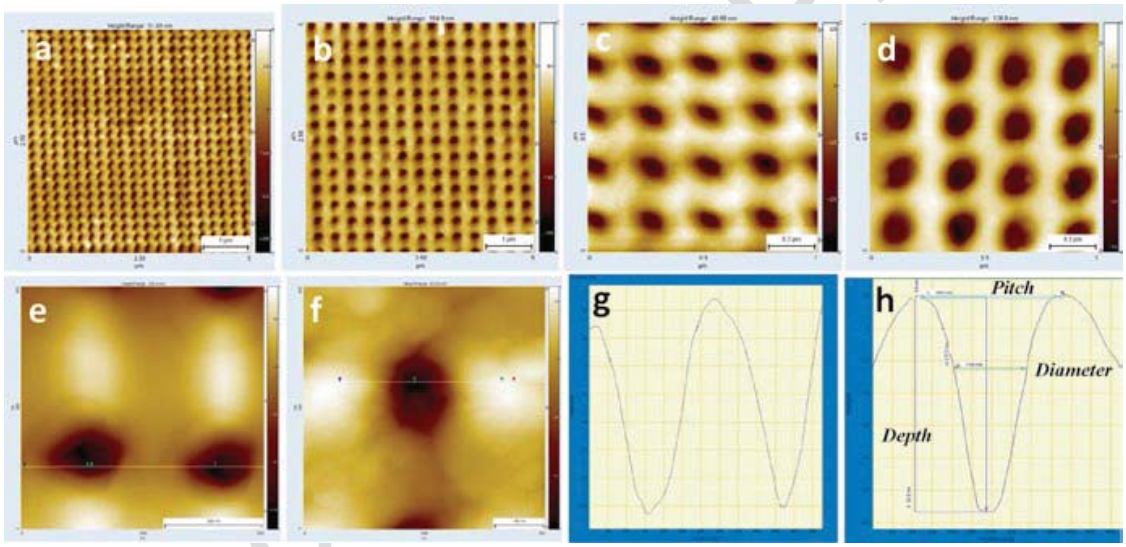

Fig. 16.14 AFM topographies of uniformly fabricated structures of (**a**, **c**, **e**) pits design A and (**b**, **d**, **f**) design B pits reproduced within the triangular areas (scale: 5×5 µm, 1×1 µm and 500×500 nm). Panels (**g**) and (**h**) represent the AFM profiles of (**e**) and (**f**) across the length of 500 nm

Smaller areas of about $150 \times 150\ \mu m^2$ showed circular shapes when imaged in top-down direction in the whole patterned area in the preliminary tests.

However, from the AFM images the shapes of the pits in design A in triangular areas are more elliptical (Fig. 16.14a, c, e), whereas those of design B are closer to perfect holes (Fig. 16.14b, d, f). The pit structures for designs A and B outside the triangular areas exhibited deformed circular shapes as demonstrated in Fig. 16.15a, b. From the stigmated nature one can conclude that there are problems with the focusing and astigmatism caused by the FIB optics. This is not surprising as the 200 times magnification is close to the lower limit of the FIB Helios column.

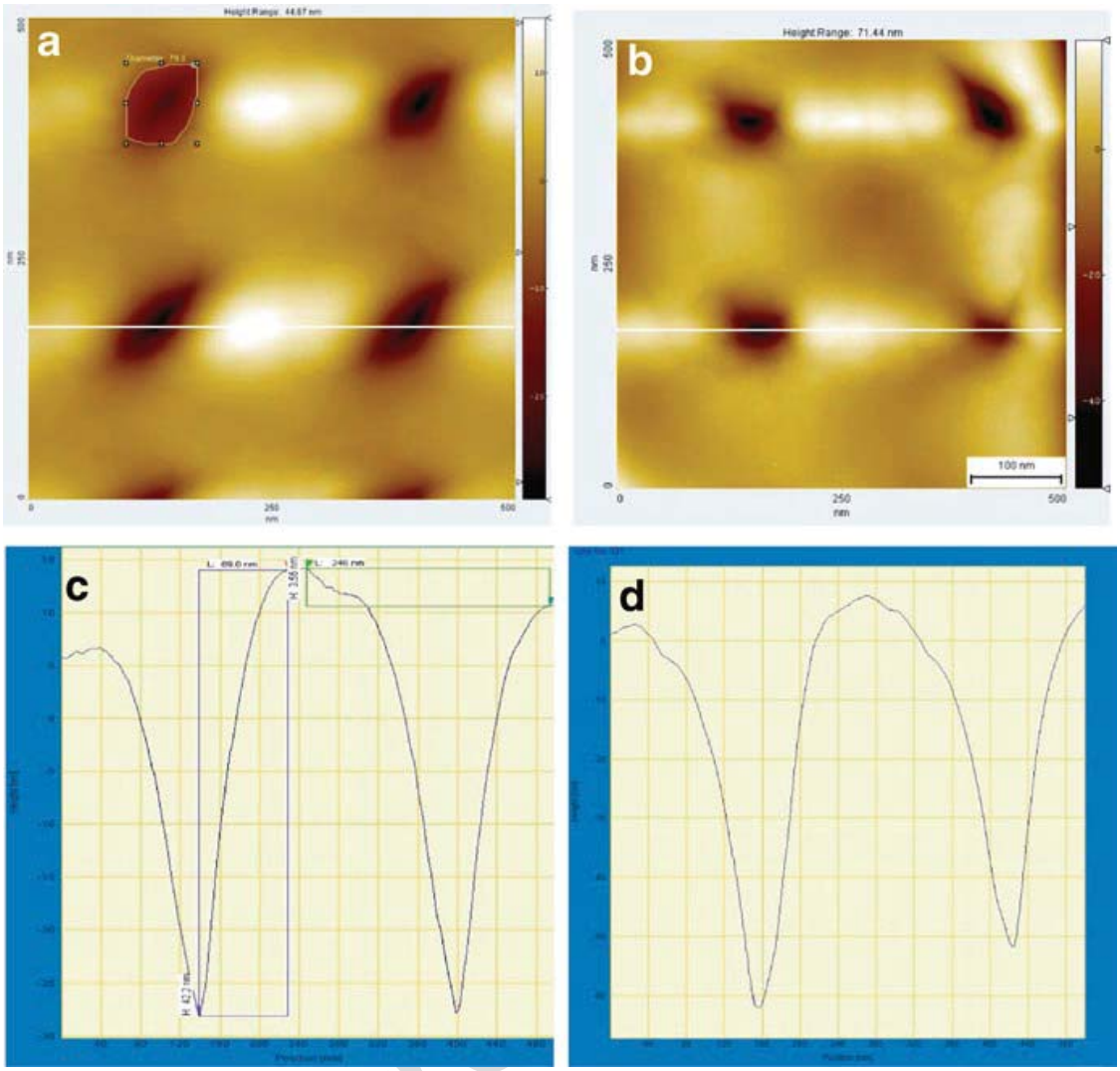

Fig. 16.15 AFM pictures of unevenly patterned pit structures of (**a** and **b**) designs A and design B reproduced outside the triangular areas (scale: 500 × 500 nm) and (**c** and **d**) profiles of (**a**) and (**b**) across the length of 500 nm

From the AFM profiles, the uniformity and distribution of the pits A and B parameters (or dimensions) such as diameter, depth and pitch produced by FIB technique were evaluated. The A and B pit dimensions were measured using a Nanoscope imaging probe software as described above.

The distribution curves of A and B pit dimensions were plotted and presented in Fig. 16.16. Figure 16.16a shows that when seeking to produce design A diameter pits ($N = 162$), the result was far from uniform. Although the highest number of pits did fall within the 116–120 nm range, the graph shows there were considerable variations in resulting pit sizes.

In seeking to produce design B diameter pits ($N = 90$), Fig. 16.16b shows a similar pattern to the result shown in the previous graph. The highest number of pits was between 181 and 185 nm range with the lowest amount of pits registering in the ranges above 180 nm.

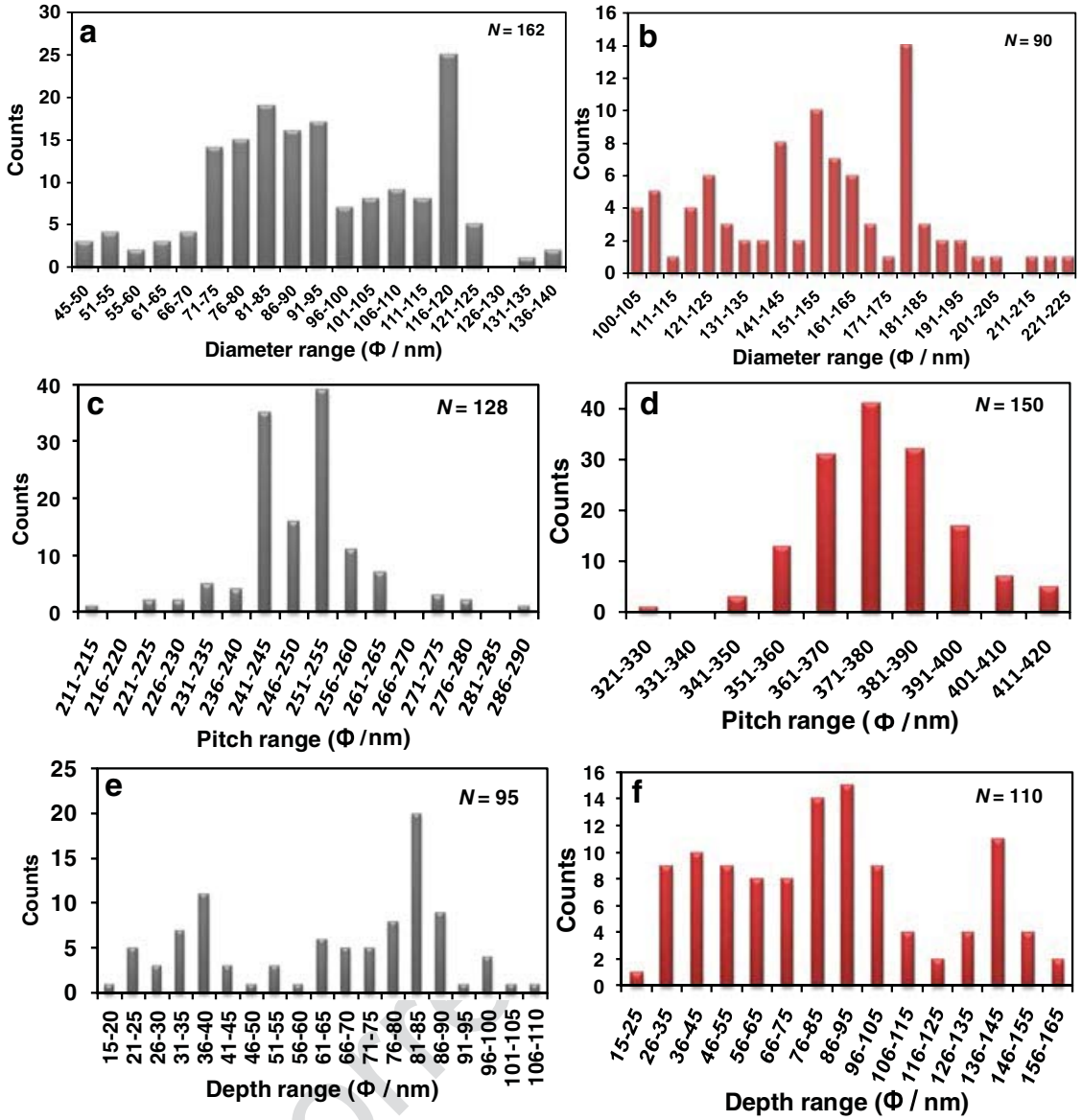

Fig. 16.16 Distribution curves of pit diameter of (**a**) and (**b**) 120 and 180 nm with a pitch of (**c**) and (**d**) 240 and 360 nm and depth of (**e**) and (**f**) 50–100 nm

The required A pitch range here (Fig. 16.16c) was 240 nm ($N=128$). Most pits registered between 251–255 and 241–245 nm then at 246–250 nm range. However, only four pits were reported at 240 nm.

In looking for a design B pitch level of 360 nm ($N=150$ nm) presented in Fig. 16.16d, only 13 pits fell within this range. The majority of pits registered at pitches higher than the required level of 360 nm, falling between 371 and 380 nm, and one pit range as high as 411–420 nm.

In searching for a design A depth of 50 or 100 nm ($N=95$), Fig. 16.16e shows that one pit reported at 46–50 nm range and four pits reported at 96–105 nm range. However, considerable variation is still noted in the dimensions of all pits.

Again looking for a design B depth of 50 or 100 nm ($N=110$), nine pits were recorded within the 46–55 nm range (Fig. 16.16f). Nine were found to have a depth

t2.1 **Table 16.2** Dimensions of 120 nm pits obtained with FIB patterning

t2.2 t2.3 Dimensions	Sites number	Mean ± SD (nm)	Lowest dimension value (nm)	Highest dimension value (nm)
t2.4 Diameter	$N = 162$	97 ± 8.5	46	138
t2.5 Pitch	$N = 128$	250 ± 11	213	290
t2.6 Depth	$N = 95$	65 ± 24	19	116

t3.1 **Table 16.3** Dimensions of 180 nm pits obtained with FIB patterning

t3.2 t3.3 Dimensions	Sites number	Mean ± SD (nm)	Lowest dimension value (nm)	Highest dimension value (nm)
t3.4 Diameter	$N = 90$	155 ± 11	10	221
t3.5 Pitch	$N = 150$	375 ± 14	323	411
t3.6 Depth	$N = 110$	84 ± 36	15	165

in the 96–105 nm range. However, some pits were also recorded above the desired 100 nm range which should have minor influence as long as they are deep enough to influence the cell adhesion.

The variations in pit dimensions demonstrated that FIB milling rate is greatly influenced by the polycrystalline structure of stainless steel and beam quality.

Tables 16.2 and 16.3 summarise the obtained pit dimensions of design A and B diameter ($N = 162$ and 90; scan area, 1×1 μm^2) and pitch and depth ($N = 128$ and 150 and 95 and 90; scan area, 5×5 μm^2) created by FIB milling. For the required 120 nm pit, the average pit had a diameter of 97 ± 8.5 nm ($N = 162$), pitch of 250 ± 11 nm ($N = 128$) and depth of 65 ± 24 nm ($N = 95$), whereas for the 180 nm pit, the average pit had a diameter of 155 ± 11 nm ($N = 90$), pitch of 375 ± 14 nm ($N = 150$) and depth of 84 ± 36 nm ($N = 110$).

Nevertheless, correlation of FIB–SEM and AFM cross-sectional imaging with the top-down appearance of known patterned area (grain) was essential in establishing accurate size and shape distribution of the formed pit structures.

All these variations in pit dimensions reported in stainless steel samples can be due to the atomic arrangement or random orientation of crystallographic structures and nonuniformity in grain size, though the shape of the incident beam at the point of impact on the sample surface will have the greatest effect of all the factors, followed by the crystallographic orientation of the grain at the surface.

16.12 In Vitro Cell Studies: Endothelial Cell Adhesion Tests

Finally, in vitro human EC culture and EC adhesion and densities studies were performed on unpolished, electropolished and nano-textured stainless steel surfaces.

Figure 16.17 shows the fluorescence images of the EC adhesion and densities after 1–5 days on unpolished, electropolished and design A and B surfaces. Very little significant difference in EC adhesion between these surfaces is revealed.

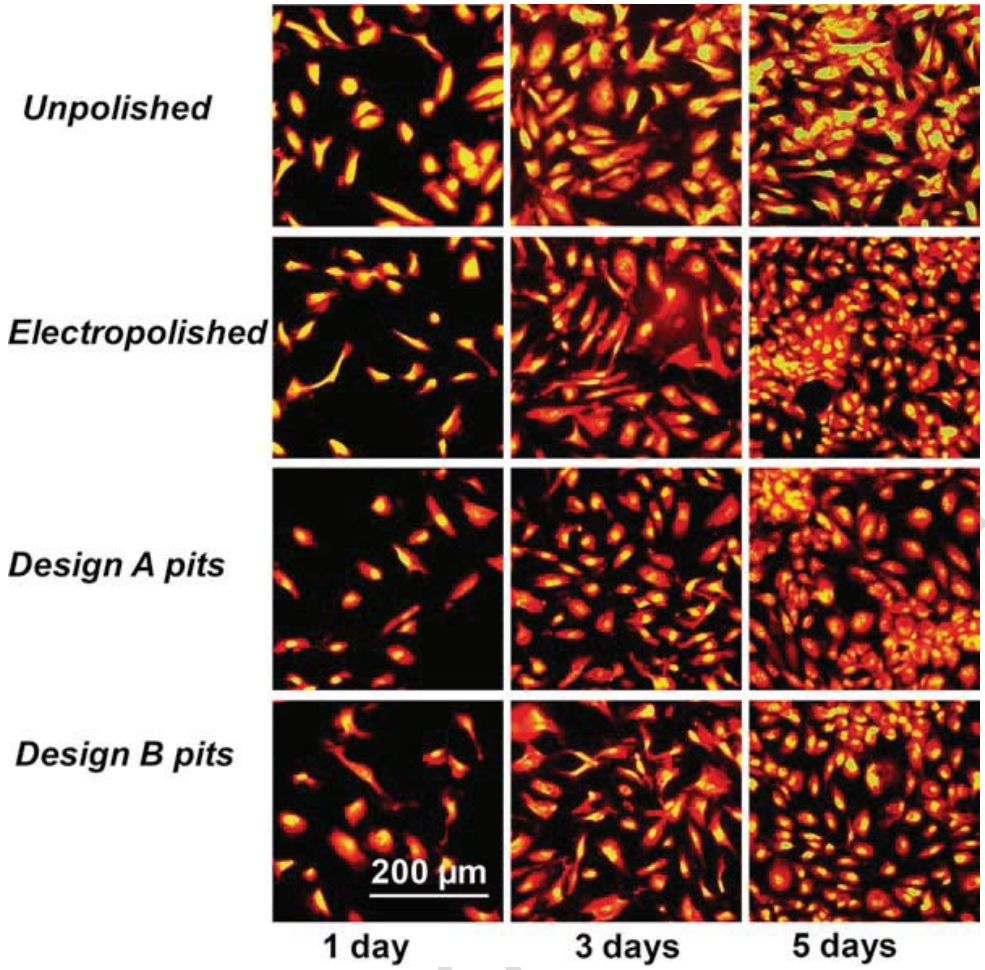

Fig. 16.17 Fluorescent images of EC cultured on (**a**) unpolished (**b**) electropolished, (**c**) design A pits and (**d**) design B pits on stainless steel surfaces after 1, 3 and 5 days

476 However, the morphology of ECs appears to be greatly defined on pits design A and
477 B relative to electropolished and unpolished samples. After 1 day, EC densities
478 were significantly lower on nano-structured 316L steel substrates when compared
479 to unpolished and electropolished control samples. EC adhesion density was signifi-
480 cantly greater after 5 days compared to 1 day for all substrates tested.
481 To confirm the significant difference in EC adhesion and densities after 1–5 days
482 involving these surfaces as demonstrated by fluorescence data, EC counts were
483 performed on each three substrate of interest ($N = 12$).

484 16.13 Conclusion

485 FIB has compelling advantages for flexible prototyping compared to other tradi-
486 tional techniques; however, the milling rates and the corresponding shape and size
487 of the formed structures are largely affected by the grain size of the polycrystalline

316L stainless steel and stability of the ion beam quality over large areas. Moreover this method is practically limited to 120 nm resolution for the desired pit depth and uniform scan size of 200 μm × 200 μm. Nevertheless formed structures show large variation of pit depths and shapes and as such surfaces might serve as a resourceful platform for screening large variations of cell/pattern stainless steel interactions. However, the FIB nano-pits design A and B created on polycrystalline stainless steel surfaces demonstrated low EC adhesion and proliferation relative to unpolished and electropolished specimens. There was no significant difference in EC adhesion and proliferation between unpolished–electropolished samples and design A and B pits. Further morphological examination of EC response on nano-structured steel surfaces would verify the mechanism for low EC adhesion and proliferation on these surfaces. Nano-patterning the stainless steel surfaces by FIB is time consuming and expensive, especially when patterning large areas. The precision and reproducibility of this technique is greatly affected by the polycrystallinity of stainless steel and a stable beam quality over large sample areas.

Acknowledgements This work was supported through a Starting Investigator Research Grant (09/SIRG/I1621) of the Science Foundation Ireland (SFI), the National Biophotonics and Imaging Platform, Ireland (NBIPI) and the Integrated NanoScience Platform for Ireland (INSPIRE) initiatives funded by the Irish Government's Programme for Research in Third Level Institutions, Cycle 4, National Development Plan 2007–2013. The authors are grateful to Dr Shanthi Muttukrishna (Department of Obstetrics and Gynaecology, University College Cork) for the gift of the human umbilical vein endothelial vein. Dr Lynette Keeney is gratefully acknowledged for performance of the AFM scans and line profiles for the correlative microscopy part of this chapter. Dr Calum Dickinson is gratefully acknowledged for contributing the EBSD measurements.

References

1. Dugdale, D.C.: Stent, in Medicine Plus, 2012. http://www.nlm.nih.gov/medlineplus/ency/article/002303.htm
2. Balamurugan, A., Rajeswari, S., Balossier, G., Rebelo, A.H.S., Ferreira, J.M.F.: Corrosion aspects of metallic implants—an overview. Mater. Corrosion **59**(11), 855–869 (2008)
3. O'Brien, B., Carroll, W.: The evolution of cardiovascular stent materials and surfaces in response to clinical drivers: a review. Acta Biomater. **5**(4), 945–958 (2009)
4. Clerc, C.O., Jedwab, M.R., Mayer, D.W., Thompson, P.J., Stinson, J.S.: Assessment of wrought ASTM F1058 cobalt alloy properties for permanent surgical implants. J. Biomed. Mater. Res. **38**(3), 229–234 (1997)
5. Craig, C., Friend, C., Edwards, M., Cornish, L., Gokcen, N.: Mechanical properties and microstructure of platinum enhanced radiopaque stainless steel (PERSS) alloys. J. Alloys Compd. **361**(1), 187–199 (2003)
6. Craig, C., Friend, C., Edwards, M., Gokcen, N.: Tailoring radiopacity of austenitic stainless steel for coronary stents. In: Medical Device Materials: Proceedings from the Materials & Processes for Medical Devices Conference 2003, 8–10 September 2003, Anaheim, California. 2004. American Society for Metals
7. Heublein, B., Rohde, R., Kaese, V., Niemeyer, M., Hartung, W., Haverich, A.: Biocorrosion of magnesium alloys: a new principle in cardiovascular implant technology? Heart **89**(6), 651–656 (2003)

8. Lüscher, T.F., Steffel, J., Eberli, F.R., Joner, M., Nakazawa, G., Tanner, F.C., Virmani, R.: Drug-eluting stent and coronary thrombosis biological mechanisms and clinical implications. Circulation **115**(8), 1051–1058 (2007)
9. Daemen, J., Wenaweser, P., Tsuchida, K., Abrecht, L., Vaina, S., Morger, C., Kukreja, N., Jüni, P., Sianos, G., Hellige, G.: Early and late coronary stent thrombosis of sirolimus-eluting and paclitaxel-eluting stents in routine clinical practice: data from a large two-institutional cohort study. Lancet **369**(9562), 667–678 (2007)
10. Chou, L., Firth, J.D., Uitto, V.-J., Brunette, D.M.: Substratum surface topography alters cell shape and regulates fibronectin mRNA level, mRNA stability, secretion and assembly in human fibroblasts. J. Cell Sci. **108**(4), 1563–1573 (1995)
11. Boyan, B.D., Hummert, T.W., Dean, D.D., Schwartz, Z.: Role of material surfaces in regulating bone and cartilage cell response. Biomaterials **17**(2), 137–146 (1996)
12. Craighead, H.G., James, C.D., Turner, A.M.P.: Chemical and topographical patterning for directed cell attachment. Curr. Opin. Solid State Mater. Sci. **5**(2–3), 177–184 (2001)
13. Curtis, A., Wilkinson, C.: Nantotechniques and approaches in biotechnology. Trends Biotechnol. **19**(3), 97–101 (2001)
14. Koegler, P., Clayton, A., Thissen, H., Santos, G.N.C., Kingshott, P.: The influence of nanostructured materials on biointerfacial interactions. Adv. Drug Deliv. Rev. **64**(15), 1820–1839 (2012)
15. Nikkhah, M., Edalat, F., Manoucheri, S., Khademhosseini, A.: Engineering microscale topographies to control the cell–substrate interface. Biomaterials **33**(21), 5230–5246 (2012)
16. Chen, L., Han, D., Jiang, L.: On improving blood compatibility: from bioinspired to synthetic design and fabrication of biointerfacial topography at micro/nano scales. Colloids Surf. B Biointerfaces **85**(1), 2–7 (2011)
17. Gentile, F., Tirinato, L., Battista, E., Causa, F., Liberale, C., di Fabrizio, E.M., Decuzzi, P.: Cells preferentially grow on rough substrates. Biomaterials **31**(28), 7205–7212 (2010)
18. Kasemo, B.: Biological surface science. Surf. Sci. **500**(1–3), 656–677 (2002)
19. Duncan, A.C., Weisbuch, F., Rouais, F., Lazare, S., Baquey, C.: Laser microfabricated model surfaces for controlled cell growth. Biosens. Bioelectron. **17**(5), 413–426 (2002)
20. Berry, C.C., Campbell, G., Spadiccino, A., Robertson, M., Curtis, A.S.G.: The influence of microscale topography on fibroblast attachment and motility. Biomaterials **25**(26), 5781–5788 (2004)
21. Yim, E.K.F., Leong, K.W.: Significance of synthetic nanostructures in dictating cellular response. Nanomedicine **1**(1), 10–21 (2005)
22. Falconnet, D., Csucs, G., Grandin, H.M., Textor, T.: Surface engineering approaches to micropattern surfaces for cell-based assays. Biomaterials **27**(16), 3044–3063 (2006)
23. Yu, L.M.Y., Leipzig, N.D., Shoichet, M.S.: Promoting neuron adhesion and growth. Mater. Today **11**(5), 36–43 (2008)
24. Roach, P., Parker, T., Gadegaard, N., Alexander, M.R.: Surface strategies for control of neuronal cell adhesion: a review. Surf. Sci. Rep. **65**(6), 145–173 (2010)
25. Nazneen, F., Herzog, G., Arrigan, D.W., Caplice, N., Benvenuto, P., Galvin, P., Thompson, M.: Surface chemical and physical modification in stent technology for the treatment of coronary artery disease. J. Biomed. Mater. Res. B Appl. Biomater. **100**, 1989–2014 (2012)
26. Norman, J.J., Desai, T.A.: Methods for fabrication of nanoscale topography for tissue engineering scaffolds. Ann. Biomed. Eng. **34**(1), 89–101 (2006)
27. Buzea, C., Beydaghyan, G., Elliott, C., Robbie, K.: Control of power law scaling in the growth of silicon nanocolumn pseudo-regular arrays deposited by glancing angle deposition. Nanotechnology **16**(10), 1986 (2005)
28. Dolatshahi-Pirouz, A., Hovgaard, M.B., Rechendorff, K., Chevallier, J., Foss, M., Besenbacher, F.: Scaling behavior of the surface roughness of platinum films grown by oblique angle deposition. Phys. Rev. B **77**(11), 115427 (2008)
29. Tseng, A.A., Notargiacomo, A.: Nanoscale fabrication by nonconventional approaches. J. Nanosci. Nanotechnol. **5**(5), 683–702 (2005)

30. Sarkar, S., Dadhania, M., Rourke, P., Desai, T.A., Wong, J.Y.: Vascular tissue engineering: microtextured scaffold templates to control organization of vascular smooth muscle cells and extracellular matrix. Acta Biomater. **1**(1), 93–100 (2005)
31. Houtchens, G.R., Foster, M.D., Desai, T.A., Morgan, E.F., Wong, J.Y.: Combined effects of microtopography and cyclic strain on vascular smooth muscle cell orientation. J. Biomech. **41**(4), 762–769 (2008)
32. Biela, S.A., Su, Y., Spatz, J.P., Kemkemer, R.: Different sensitivity of human endothelial cells, smooth muscle cells and fibroblasts to topography in the nano–micro range. Acta Biomater. **5**(7), 2460–2466 (2009)
33. Green, A.M., Jansen, J.A., Van der Waerden, J.P.C.M., Von Recum, A.F.: Fibroblast response to microtextured silicone surfaces: texture orientation into or out of the surface. J. Biomed. Mater. Res. **28**(5), 647–653 (1994)
34. Walboomers, X., Croes, H., Ginsel, L., Jansen, J.: Contact guidance of rat fibroblasts on various implant materials. J. Biomed. Mater. Res. **47**(2), 204–212 (1999)
35. Walboomers, X., Croes, H., Ginsel, L., Jansen, J.: Growth behavior of fibroblasts on microgrooved polystyrene. Biomaterials **19**(20), 1861–1868 (1998)
36. Walboomers, X., Ginsel, L., Jansen, J.: Early spreading events of fibroblasts on microgrooved substrates. J. Biomed. Mater. Res. **51**(3), 529–534 (2000)
37. Walboomers, X., Monaghan, W., Curtis, A., Jansen, J.: Attachment of fibroblasts on smooth and microgrooved polystyrene. J. Biomed. Mater. Res. **46**(2), 212–220 (1999)
38. Loesberg, W.A., te Riet, J., van Delft, F.C., Schön, P., Figdor, C.G., Speller, S., van Loon, J.J., Walboomers, X.F., Jansen, J.A.: The threshold at which substrate nanogroove dimensions may influence fibroblast alignment and adhesion. Biomaterials **28**(27), 3944–3951 (2007)
39. Dalby, M.J., Gadegaard, N., Riehle, M.O., Wilkinson, C.D.W., Curtis, A.S.G.: Investigating filopodia sensing using arrays of defined nano-pits down to 35 nm diameter in size. Int. J. Biochem. Cell Biol. **36**(10), 2005–2015 (2004)
40. Dalby, M.J., Gadegaard, N., Wilkinson, C.D.: The response of fibroblasts to hexagonal nanotopography fabricated by electron beam lithography. J. Biomed. Mater. Res. A **84**(4), 973–979 (2008)
41. Yim, E.K.F., Reano, R.M., Pang, S.W., Yee, A.F., Chen, C.S., Leong, K.W.: Nanopattern-induced changes in morphology and motility of smooth muscle cells. Biomaterials **26**(26), 5405–5413 (2005)
42. Lee, S.W., Kim, S.Y., Rhyu, I.C., Chung, W.Y., Leesungbok, R., Lee, K.W.: Influence of microgroove dimension on cell behavior of human gingival fibroblasts cultured on titanium substrata. Clin. Oral Implants Res. **20**(1), 56–66 (2009)
43. Ito, T., Okazaki, S.: Pushing the limits of lithography. Nature **406**(6799), 1027–1031 (2000)
44. Chou, S.Y., Krauss, P.R., Renstrom, P.J.: Imprint of sub-25 nm vias and trenches in polymers. Appl. Phys. Lett. **67**(21), 3114–3116 (1995)
45. Raffa, V., Castrataro, P., Menciassi, A., Dario, P.: Focused Ion Beam as a Scanning Probe: Methods and Applications. Applied Scanning Probe Methods II, pp. 361–412. Springer, New York, NY (2006)
46. Iordanova, I., Antonov, V., Gurkovsky, S.: Changes of microstructure and mechanical properties of cold-rolled low carbon steel due to its surface treatment by Nd:glass pulsed laser. Surf. Coat. Technol. **153**(2–3), 267–275 (2002)
47. Duncan, A.C., Rouais, F., Lazare, S., Bordenave, L., Baquey, C.: Effect of laser modified surface microtopochemistry on endothelial cell growth. Colloids Surf. B Biointerfaces **54**(2), 150–159 (2007)
48. Kalantar-Zadeh, K., Fry, B.: Nanotechnology Enabled Sensors. Springer, New York, NY (2007)
49. Volkert, C., Minor, A.: Focused ion beam microscopy and micromachining. MRS Bull. **32**(5), 389–395 (2007)
50. Lanyon, Y.H., De Marzi, G., Watson, Y.E., Quinn, A.J., Gleeson, J.P., Redmond, G., Arrigan, D.W.: Fabrication of nanopore array electrodes by focused ion beam milling. Anal. Chem. **79**(8), 3048–3055 (2007)

51. Choi, C.H., Heydarkhan-Hagvall, S., Wu, B.M., Dunn, J.C., Beygui, R.E., Kim, C.J.: Cell growth as a sheet on three-dimensional sharp-tip nanostructures. J. Biomed. Mater. Res. A **89**(3), 804–817 (2009)
52. Raffa, V., Vittorio, O., Pensabene, V., Menciassi, A., Dario, P.: FIB-nanostructured surfaces and investigation of bio/nonbio interactions at the nanoscale. IEEE Trans. NanoBiosci. **7**(1), 1–10 (2008)
53. Joshi, K., Singh, P., Verma, S.: Fabrication of platinum nanopillars on peptide-based soft structures using a focused ion beam. Biofabrication **1**(2), 025002 (2009)
54. Choubey, A., Marton, D., Sprague, E.A.: Human aortic endothelial cell response to 316L stainless steel material microstructure. J. Mater. Sci. Mater. Med. **20**(10), 2105–2116 (2009)
55. Misra, R.D., Nune, C., Pesacreta, T.C., Somani, M.C., Karjalainen, L.P.: Understanding the impact of grain structure in austenitic stainless steel from a nanograined regime to a coarse-grained regime on osteoblast functions using a novel metal deformation–annealing sequence. Acta Biomater. **9**, 6245–6258 (2013)
56. Russell, A., Lee, K.L.: Structure-Property Relations in Nonferrous Metals. Wiley-Interscience, New York, NY (2005)
57. Shi, D.: Introduction to Biomaterials. World Scientific, London (2006)
58. Nazneen, F., Galvin, P., Arrigan, D.W., Thompson, M., Benvenuto, P., Herzog, G.: Electropolishing of medical-grade stainless steel in preparation for surface nano-texturing. J. Solid State Electrochem. **16**(4), 1389–1397 (2012)
59. Dalby, M.J., Berry, C.C., Riehle, M.O., Sutherland, D.S., Agheli, H., Curtis, A.S.G.: Attempted endocytosis of nano-environment produced by colloidal lithography by human fibroblasts. Exp. Cell Res. **295**(2), 387–394 (2004)
60. Schmidt, M., Nazneen, F., Georgiev, Y., Herzog, G., Galvin, P., Petkov, N.: FIB patterning of stainless steel for the development of nano-structured stent surfaces for cardiovascular applications. J. Phys. Conf. **371**(1), 012065 (2012)
61. Nazneen, F., Schmidt, M., McLoughlin, E., Petkov, N., Herzog, G., Arrigan, D., Galvin, P.: Nano-texturing of medical-grade 316L stainless steel by focused ion beam for endothelial cell studies. J. Nanosci. Nanotechnol., 2013. [AU4]
62. Feitknecht, W.: Über den angriff von krystallen durch kanalstrahlen. Helv. Chim. Acta **7**(1), 825–842 (1924)
63. Wehner, G.K.: Controlled sputtering of metals by low-energy Hg ions. Phys. Rev. **102**(3), 690–704 (1956)
64. Wehner, G.K., Rosenberg, D.: Angular distribution of sputtered material. J. Appl. Phys. **31**(1), 177–179 (1960)
65. Sigmund, P.: Theory of sputtering. I. Sputtering yield of amorphous and polycrystalline targets. Phys. Rev. **184**(2), 383–416 (1969)
66. Bean, K.E.: Anisotropic etching of silicon. IEEE Trans. Electron Dev. **25**(10), 1185–1193 (1978)
67. Seidel, H., Csepregi, L., Heuberger, A., Baumgärtel, H.: Anisotropic etching of crystalline silicon in alkaline solutions I. Orientation dependence and behavior of passivation layers. J. Electrochem. Soc. **137**(11), 3612–3626 (1990)
68. Schmidt, M., Nazneen, F., Herzog, G., Arrigan, D., Galvin, P., Keeney, L., Petkov, N., Holmes, J.D.: to be submitted. [AU5]
69. Schmidt, M., Nazneen, F., Herzog, G., Arrigan, D., Galvin, P., Dickinson, C., de Silva, J.P., Scanlan, D., O'Hara, N., Cross, G.L.W.: Correlative microscopy study of FIB patterned stainless steel surfaces as novel nano-structured stents for cardiovascular applications. MRS Proc 2012. 1466(1). [AU6]
70. Giannuzzi, L., Stevie, F.: A review of focused ion beam milling techniques for TEM specimen preparation. Micron **30**(3), 197–204 (1999)
71. Schwartz, A.J., Kumar, M., Adams, B.L., Field, D.P.: Electron Backscatter Diffraction in Materials Science. Springer, New York, NY (2009)
72. Stark, Y., Fromter, R., Stickler, D., Oepen, H.P.: Sputter yields of single-and polycrystalline metals for application in focused ion beam technology. J. Appl. Phys. **105**(1), 013542-1–013542-5 (2009)